Probing Planck's Law with Incandescent Light Emission from a Single Carbon Nanotube

Yuwei Fan, S. B. Singer, Raymond Bergstrom, and B. C. Regan*

Department of Physics and Astronomy, University of California, Los Angeles, California, 90095 and California NanoSystems Institute, Los Angeles, California, 90095

(Received 18 January 2009; published 5 May 2009)

We present thermal and electron micrographs of an incandescent lamp constructed from a multiwalled carbon nanotube, and correlate the subwavelength optical information with the underlying nanoscopic structure. Remarkably, the heat equation and Planck's law together give a precise, quantitative description of the light intensity as a function of input power, even though the nanotube's small size places it outside the thermodynamic limit.

DOI: 10.1103/PhysRevLett.102.187402 PACS numbers: 82.60.Qr, 05.30.−d, 65.80.+n, 78.67.Ch

Planck's derivation of the spectrum of a blackbody radiator in 1900 introduced the quantum hypothesis, which ultimately led to the development of quantum mechanics a quarter century later. Despite determined efforts by generations of physicists, the connection between quantum mechanics and thermodynamics is still not understood [1]. Recent progress includes a new demonstration of how quantum entanglement leads to thermodynamic entropy [2], and the successful application of nanothermodynamics [3] to an outstanding problem in ferromagnetism [4]. The ''nano'' prefix gives an appropriate description of the relevant size scale, for the intersection of the realms of quantum mechanics and thermodynamics occurs in small systems. In this Letter we report imaging a small, but not pointlike, radiator constructed to probe this boundary.

The classical blackbody source is a cavity with linear size dimension l at temperature T that emits, through a hole of size a, radiation of characteristic wavelength λ_c. In the thermodynamic limit the three length scales are related by $l \gg a \gg \lambda_c$ [5]. In our experiment we drive an electrical current through a carbon nanotube of length L and radius r suspended over a gap in a silicon substrate. The central portion of the nanotube, brought to high temperature by Joule heating, radiates such that $\lambda_c \sim L \gg r$. With one length scale on the boundary and the other deep in the quantum limit, this radiator has an ideal geometry for testing the Planckian model.

As lamps, carbon nanotubes have the additional advantage that they are anticipated to be among the most temperature-stable materials [6]. Thermal radiation has been observed from a variety of carbon nanostructures, including carbon clusters [7], soot [8], nanotubes [9–13], and fullerenes [14–16]. These last experiments illustrate some of the unsolved problems in this intermediate regime, for the relationship between the fullerene's temperature and its emitted radiation is not well understood [14,15,17].

Our device construction [18,19] allows the lamp to be imaged with atomic resolution inside a transmission electron microscope (TEM). A completed device consists of an arc-discharge grown, multiwalled carbon nanotube (MER Corporation) on a 12 nm thick Si_3N_4 membrane that spans a hole in a 2 mm × 2 mm × 0.2 mm silicon chip. The nanotube is contacted with 80 nm of Au over 50 nm of Pd [20] using e-beam lithography.

We image the device in a TEM (FEI Titan 80–300) at 80 kV, under applied bias in an optical microscope, and then again in the TEM. The optical microscope is designed to achieve the maximum possible resolution consistent with the constraints imposed by having the lamp in vacuum ($\sim 2 \times 10^{-7}$ torr). Spherical aberration from the vacuum window, 1.1 mm of BK-7 glass, is avoided through use of a corrected microscope objective (100 ×, NA 0.5). The only other optical components in the light path are one of eleven 10 nm bandpass filters, swapped with motorized filter wheels, and the tube lens. The light is detected with a low-noise, high quantum efficiency, 1 megapixel silicon CCD cooled to −70 °C.

Representative image data are shown in Fig. 1. The device pictured has been chosen for presentation because its exceptional stability allowed for many measurements under nearly identical conditions. In the ''before'' TEM image a single nanotube spans the 1.3 μm gap between two electrodes on a relatively clean and uniform membrane. Comparison with the ''after'' TEM image shows damage to the membrane, with marked thinning near the center of the nanotube. Regions with now darker contrast toward the edge of the characteristic [18,19] damage pattern have perhaps acquired some of this removed material via surface migration. These images show that this nanotube supported a large thermal gradient, with the peak temperature occurring near its midpoint.

The optical data confirm these basic facts. By back-illuminating the membrane while the nanotube is also emitting, we establish the position of the hot spot relative to features on the membrane. Subsequent pyrometric images are taken with no light sources other than the nanotube. Comparing images pairwise in the sequence ''nanotube only'', ''backlight with nanotube'', ''backlight only'', ''low magnification TEM'', ''high magnification TEM'', we construct the composite image Fig. 2. The overlay algorithm allows for scaling, rotation, horizontal shift, and ver-

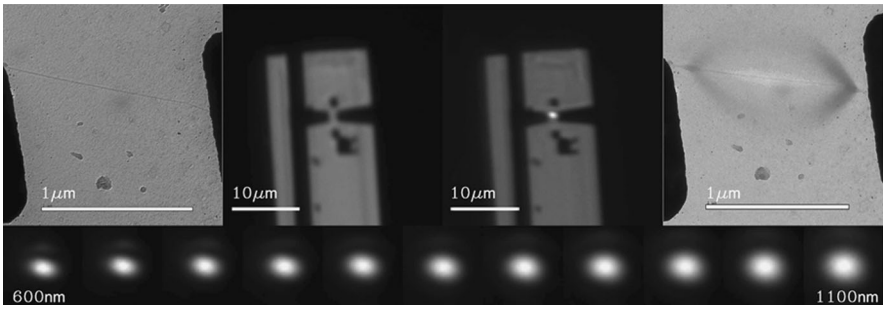

FIG. 1. The carbon nanotube lamp. The four upper images from left to right are "before" (TEM), "backlight only" (optical), "backlight with nanotube" (optical), and "after"(TEM). The 4 μm $\times$ 4 μm lower images are 4.7 V bias "nanotube only", taken with bandpass filters centered at wavelengths 600–1100 nm (50 nm increments). The lamp is visible to the unaided eye. Higher resolution TEM images (not shown) indicate that the 1.4 μm long nanotube has 11 walls and an outer diameter of 13 nm.

tical shift, and puts the images in register to better than 30 nm.

To understand the light emission from the nanotube, we start by assuming the heat equation is valid [21]. Neglecting the Thomson effect and conduction by the membrane, the distribution of T in a wire carrying current I is described by

$$c' \frac{\partial T}{\partial t} = \frac{\partial}{\partial x}\left(\kappa A \frac{\partial}{\partial x} T\right) + I^2 \frac{\rho}{A} + \epsilon C \sigma (T_0^4 - T^4), \quad (1)$$

where c' is the wire's heat capacity per unit length, κ is the thermal conductivity, A is its effective cross-sectional area, ρ is the electrical resistivity, ϵ is the wire emissivity, C is its effective circumference for radiation, σ is the Stephan-Boltzmann radiation constant, and T_0 is the radiation temperature of the environment.

The thermal conduction and Joule heating terms are overwhelmingly dominant in our situation. The tiny system reaches the steady-state condition in $\lesssim$100 ns, so we consider the case $\frac{\partial T}{\partial t} = 0$. While the radiation is the key observable, the far-field radiated power $\propto T^4$ has negligible effect on the temperature distribution. Dimensional analysis shows that the crossover temperature T_x from a conduction-dominated to a radiation-dominated regime scales like $T_x \sim \sqrt[3]{\kappa/\epsilon\sigma\delta}$, where δ is a length scale. For nanotubes, which are both excellent thermal conductors and very small, T_x is tens of thousands of Kelvin.

To get an analytic approximation for $T(x)$, we take ρ and κ to be constant, and neglect the radiation term. With boundary conditions $T(x = \pm L/2) = T_0$, the resulting second-order equation has the solution

$$T(x) = T_{\max} + (T_0 - T_{\max})\left(\frac{2x}{L}\right)^2, \quad (2)$$

a parabola, where

$$T_{\max} = T_0 + I^2 \rho L^2 / 8\kappa A^2 = T_0 + \alpha P. \quad (3)$$

More generally, for temperature independent $\rho/\kappa \propto \delta(x)$ or $|x|^m$ $(m \geq 0)$ the temperature increment $\Delta T \equiv T_{\max} - T_0$ is proportional to the input power $P = IV$. The temperature distribution (2) has been seen previously [13,22] in suspended carbon nanotubes.

Using (2), we can model the signal at the camera by convolving the expected signal from each portion of the nanotube with the point-spread function (PSF) of the microscope. According to Planck's law [5], the expected photon count rate Γ from a length dx of wire in bandwidth $d\lambda$ is

$$\Gamma = 2\pi\epsilon\left(\frac{c}{\lambda}\right)\left(\frac{d\lambda}{\lambda}\right)\left(\frac{C dx}{\lambda^2}\right)\frac{1}{e^{hc/\lambda kT} - 1}. \quad (4)$$

A radiating object with dimensions smaller than a wavelength violates the assumptions underpinning this law, but the resulting corrections can be accommodated with a suitable choice of the emissivity ϵ. Taking the PSF to be a Gaussian distribution [23] with standard deviation $s = 0.21\lambda/\mathrm{NA}$, where NA is the numerical aperture of the objective, we arrive at an approximate expression for the photoelectron count rate $\dot{S}$ at camera pixel (i, j),

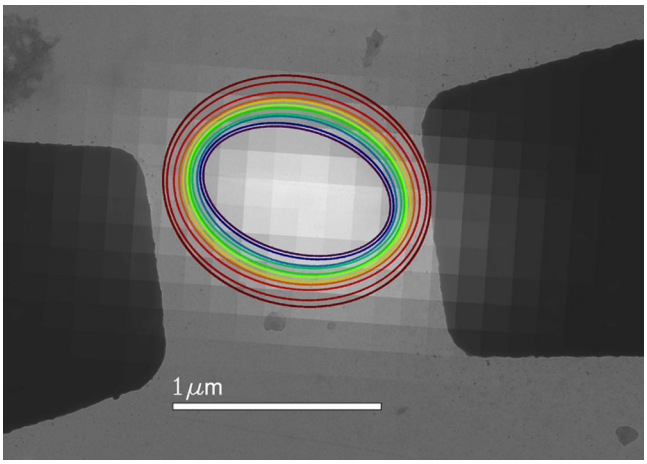

FIG. 2 (color online). Composite overlay constructed from the 600 nm and post-heating TEM images shown separately in Fig. 1. The optical CCD pixels have effective linear dimension $\beta = 127$ nm. Also shown are all 11 one standard-deviation intensity boundaries implied by 2D Gaussian fits to the "nanotube only" images of Fig. 1.

$$\dot{S}(i,j) = \Phi\Theta \int_{-L/2}^{L/2} \epsilon \frac{2\pi c}{\lambda^4} \frac{C\Delta\lambda dx}{e^{hc/\lambda kT(x)} - 1} \times \frac{\beta^2 e^{((i\beta - x)^2 + (j\beta)^2)/-2s^2}}{2\pi s^2}, \quad (5)$$

where Φ and Θ ($\Phi\Theta \sim 10^{-2}$) are geometric and quantum collection efficiencies, $\Delta\lambda$ is the effective bandwidth of an optical filter, and β is the CCD pixel linear dimension divided by the optical magnification.

The integral (5) can be easily computed numerically, but an analytic approximation is useful. For our experimental conditions, $hc/\lambda kT$ is large everywhere ($hc/k = 14.4\ \mu\text{m} \cdot \text{kK}$), allowing us to write

$$\frac{1}{e^{hc/\lambda kT} - 1} \sim e^{-hc/\lambda kT}(1 + e^{-hc/\lambda kT}). \quad (6)$$

Since $T_0/T_{\max}$ is small and the largest contributions to the integral come from near $x = 0$, we can also expand $T(x)$, finding

$$\frac{1}{T(x)} \sim \frac{1}{T_{\max}}\left(1 + \frac{T_{\max} - T_0}{T_{\max}}\left(\frac{2x}{L}\right)^2\right) \quad (7)$$

Extending the integration limits to $\pm\infty$ introduces negligible error and allows the integral to be performed. Dropping second-order small terms leaves the following, accurate to $\lesssim 6\%$ compared to Eq. (5) for our conditions:

$$\dot{S}(i,j) = \Phi\Theta\epsilon \frac{2\pi c}{\lambda} \frac{\Delta\lambda}{\lambda} \frac{C\beta^2}{s\lambda^2} \sqrt{\frac{1 - 1/\xi^2}{2\pi}} \quad (8a)$$

$$(1 + e^{-hc/\lambda kT_{\max}}) \quad (8b)$$

$$\times e^{-hc/\lambda kT_{\max}} e^{-(\beta^2/2s^2)((i/\xi)^2 + j^2)}, \quad (8c)$$

where

$$\xi = \sqrt{1 + \frac{\lambda k T_{\max}^2 L^2}{8hc(T_{\max} - T_0)s^2}}. \quad (9)$$

The two important implications of expression (8) are captured on (8c). First, a given image's intensity distribution is an elliptical Gaussian, with its long axis parallel to the nanotube and eccentricity $\sqrt{1 - 1/\xi^2}$ dependent on the ratio of the nanotube length L to the microscope resolution s. We fit the optical data $\dot{S}(i,j)$ to a Gaussian with center coordinates, axes, rotation angle, amplitude and offset as free parameters. Figure 2 shows the returned ellipse parameters graphically for the 11 bandpass filters. Analyzing the semiminor axis b as a linear function of wavelength, we find $b \simeq 0.43\lambda + 30$ nm, in good agreement with the expectation $b = 0.42\lambda$ for diffraction-limited (sub-λ) resolution of a perfect line source. Thus radiation from the membrane is either weak or produced only very near the nanotube. For the semimajor axis $a \simeq 0.37\lambda + 220$ nm, demonstrating resolution of the nanotube's finite length.

The second noteworthy implication of Eq. (8) is that the maximum intensity in a given image is proportional to $e^{-hc/\lambda kT_{\max}}$. Thus, because we are in the Wien (exponential) limit, the signal intensity measures $T_{\max}$ directly, and not a spatially averaged temperature as might be expected. However, even with our sizable array of bandpass filters, accurate determination of the temperature with traditional pyrometric methods is problematic [24,25], and depends critically on the assumed form of $\epsilon(\lambda)$.

We are developing a pyrometric method which replaces the assumption, standard in multiwavelength pyrometry, of $\frac{d\epsilon}{d\lambda}$ known, with the milder assumption $\frac{d\epsilon}{dT} = 0$. The method leverages our ability to change the nanotube's temperature quickly and reproducibly, and has the significant advantage that it requires no calibration of the net optical collection efficiency $\Phi(\lambda)\Theta(\lambda)$. Moreover, it probes directly the T and h-dependent Planck factor, and is insensitive to ϵ, the classical phase space terms, and small errors in the analytic approximation (8). Taking the logarithm of Eq. (8) and using Eq. (3) yields

$$\frac{\lambda k_B}{hc} \ln\dot{S}(0,0) = \frac{1}{T_\lambda} - \frac{1}{T_0 + \alpha P}, \quad (10)$$

where T_λ, which depends on the factors of the lines (8a) and (8b), is approximately independent of P. This new variable T_λ gives an intuitive measure of the sensitivity of the apparatus to the sample, answering the question, "at what $T_{\max}$ does the nanotube produce a 1 Hz photoelectron count rate in the central CCD pixel?"

We image the nanotube of Figs. 1 and 2 with applied bias voltage 4.05–4.7 V in 50 mV steps, using the same bandpass filters as before. Figure 3 plots the left-hand side of Eq. (10) vs the average applied power P for each filter. The solid curves represent Levenberg-Marquardt fits to the right-hand side of Eq. (10), with T_λ, T_0, and α as adjustable parameters (Fig. 4). Fitting weights are calculated assuming that the only significant error source is the shot noise in the collected photoelectrons. These errors are small; using the algorithm described here, we predicted the count rates and set the exposure times τ to collect 1–6 $\times 10^4$ photo-

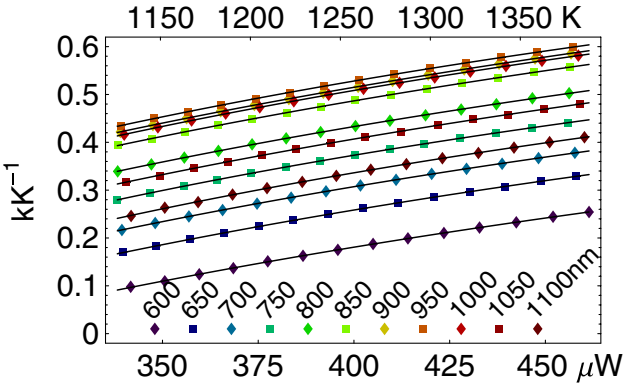

FIG. 3 (color online). The function $\frac{\lambda k_B}{hc} \ln\dot{S}(0,0)[\text{kK}^{-1}]$ vs $P[\mu\text{W}]$, for the 11 bandpass filters of central wavelengths $\lambda[\text{nm}]$. The statistical uncertainties are smaller than the symbols designating the data in all cases. The upper abscissa gives $T_{\max}[\text{K}]$ for the nanotube, assuming the global best fit values of T_0 and α.

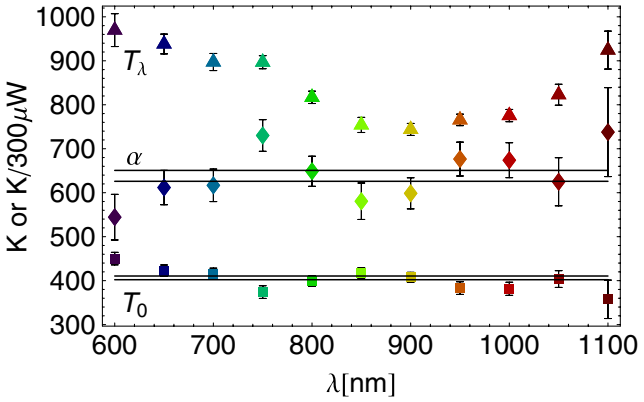

FIG. 4 (color online). Fit parameters T_λ[K], α[K/300 μW], and T_0[K] found from the data of Fig. 3, indicated by ▲, ◆, and ■, respectively, and colored as previously according to λ[nm]. α's display units have been chosen to allow this compact graphic. The weighed means, $T_0 = 406 \pm 4$ K and $\alpha = 2.13 \pm 0.04$ K/μW, are indicated by horizontal lines showing the one-standard-deviation limits. Anticorrelation between the values found for T_0 and α is clearly evident. The variation in T_λ is expected, and is largely dictated by decreasing source brightness and decreasing camera quantum efficiency at short and long wavelengths, respectively.

electrons in the peak pixel, subject to the constraint $\tau \leq 120$ s. Only the $\tau = 120$ s pictures—low-bias pictures taken with filters toward the extremes—had fractional uncertainties in the peak intensity as large as 1%.

The simple model (10) describes the data to within their statistical precision. The fits of Fig. 3 have a reduced chi-squared statistic $\chi_r^2 = 1.5 \pm 0.9$. Using measures of the peak intensity that are statistically weightier than the maximum pixel value, such as the amplitude found by a 2D Gaussian fit, results in improved agreement. Other models with the same number of free parameters are less successful: holding fixed $T_0 = 300$ K and taking $\Delta T = \alpha_1 V + \alpha_2 V^2$, etc., gives larger χ_r^2, as does taking $\Delta T \propto I$, I^2, I^3, V, V^2, or V^3 instead of IV. Thus even though the deviations of $I(V)$ from perfect linearity are less than 0.3% in the range 4.05–4.7 V, P is still preferred to functions quadratic in either I or V separately, which supports the validity of Eq. (10).

In conclusion, we have mapped a nontrivial molecular structure, radiating in the visible, with sub-λ optical microscopy. Applying thermodynamic tools to this nanoscopic system results in a pyrometric model with real predictive power: only a few measurements are necessary to determine the complete luminosity vs applied bias relationship. This result is not particular to nanotubes or high NA microscopes, but can be applied to any thermal radiator with conduction as its dominant heat loss mechanism. Further work with other thermometry techniques (e.g., Raman [22] or multi-λ pyrometry [25]) is necessary to determine how well the values found by the fitting procedure represent the true thermodynamic temperature, and how well this quantity can be defined in such a small system.

The authors thank Shaul Aloni and Adam Fennimore for their advice and assistance. This work was supported by NSF CAREER grant No. 0748880.

*regan@physics.ucla.edu

[1] L. S. Schulman, *Time's Arrows and Quantum Measurement* (Cambridge University Press, New York, 1997).
[2] S. Popescu, A. J. Short, and A. Winter, Nature Phys. **2**, 754 (2006).
[3] T. L. Hill, Nano Lett. **1**, 111 (2001).
[4] R. V. Chamberlin, Nature (London) **408**, 337 (2000).
[5] F. Reif, *Fundamentals of Statistical and Thermal Physics*, McGraw-Hill series in fundamentals of physics (McGraw-Hill, New York, 1965).
[6] K. W. Zhang, G. M. Stocks, and J. X. Zhong, Nanotechnology **18**, 285703 (2007).
[7] E. A. Rohlfing, J. Chem. Phys. **89**, 6103 (1988).
[8] A. C. Eckbreth, J. Appl. Phys. **48**, 4473 (1977).
[9] J. Q. Wei, J. L. Sun, D. H. Wu, J. H. Guo, J. B. Luo, and K. L. Wang, Chin. Phys. **15**, 2731 (2006).
[10] A. A. Zakhidov, R. Nanjundaswamy, M. Zhang, S. B. Lee, A. N. Obraztsov, and A. Cunningham, J. Appl. Phys. **100**, 044327 (2006).
[11] P. Li, K. L. Jiang, M. Liu, Q. Q. Li, S. S. Fan, and J. L. Sun, Appl. Phys. Lett. **82**, 1763 (2003).
[12] M. Sveningsson, M. Jonsson, O. A. Nerushev, F. Rohmund, and E. E. B. Campbell, Appl. Phys. Lett. **81**, 1095 (2002).
[13] D. Mann, Y. K. Kato, A. Kinkhabwala, E. Pop, J. Cao, X. R. Wang, L. Zhang, Q. Wang, J. Guo, and H. J. Dai, Nature Nanotech. **2**, 33 (2007).
[14] E. Kolodney, A. Budrevich, and B. Tsipinyuk, Phys. Rev. Lett. **74**, 510 (1995).
[15] R. Mitzner and E. E. B. Campbell, J. Chem. Phys. **103**, 2445 (1995).
[16] L. Hackermuller, K. Hornberger, B. Brezger, A. Zeilinger, and M. Arndt, Nature (London) **427**, 711 (2004).
[17] K. Hansen and E. E. B. Campbell, Phys. Rev. E **58**, 5477 (1998).
[18] T. D. Yuzvinsky, W. Mickelson, S. Aloni, S. L. Konsek, A. M. Fennimore, G. E. Begtrup, A. Kis, B. C. Regan, and A. Zettl, Appl. Phys. Lett. **87**, 083103 (2005).
[19] G. E. Begtrup, K. G. Ray, B. M. Kessler, T. D. Yuzvinsky, H. Garcia, and A. Zettl, Phys. Rev. Lett. **99**, 155901 (2007).
[20] Z. H. Chen, J. Appenzeller, J. Knoch, Y. M. Lin, and P. Avouris, Nano Lett. **5**, 1497 (2005).
[21] J. J. Greffet, in *Microscale and Nanoscale Heat Transfer*, Topics in Applied Physics Vol. 107 (Springer-Verlag, Berlin, 2007), pp. 1–13.
[22] I. K. Hsu, R. Kumar, A. Bushmaker, S. B. Cronin, M. T. Pettes, L. Shi, T. Brintlinger, M. S. Fuhrer, and J. Cumings, Appl. Phys. Lett. **92**, 063119 (2008).
[23] B. Zhang, J. Zerubia, and J. C. Olivo-Marin, Appl. Opt. **46**, 1819 (2007).
[24] A. G. Emslie and H. H. Blau, J. Electrochem. Soc. **106**, 877 (1959).
[25] P. B. Coates, Metrologia **17**, 103 (1981).